Complete characterization of a spatiotemporally complex pulse by an improved single-frame pulse-measurement technique

Zhe Guang,* Michelle Rhodes, Matt Davis, and Rick Trebino

School of Physics, Georgia Institute of Technology, 837 State Street, Atlanta, Georgia 30332, USA
*Corresponding author: zguang3@gatech.edu

We further develop a simple device, called Spatially and Temporally Resolved Intensity and Phase Evaluation Device: Full Information from a Single Hologram (STRIPED FISH), for measuring the complete spatiotemporal intensity and phase, $I(x, y, t)$ and $\phi(x, y, t)$, respectively, of an arbitrary ultrashort pulse on a single camera frame (and hence, on a single shot). We have increased the measurable bandwidth, eliminated most aberrations, and improved the uniformity of the multiple holograms in the device. We demonstrate these improvements by making single-camera-frame measurements of spatiotemporally complex subpicosecond crossed and chirped pulses from a Ti:sapphire oscillator. In order to display the massive resulting data files—pairs of four-dimensional intensity-and-phase data—we also develop a method for generating intuitive movies of the measured pulses. With these improvements, this device and its resulting movies should be able to perform and intuitively display true single-shot spatiotemporal measurements of most current ultrashort pulses.   © 2014 Optical Society of America

OCIS codes: (320.0320) Ultrafast optics; (320.7100) Ultrafast measurements.
http://dx.doi.org/10.1364/JOSAB.31.002736

1. INTRODUCTION

Ultrashort laser pulses have a wide variety of applications, from laser machining and coherent control of chemical reactions to ultrafast spectroscopy. Most such applications operate best with a pulse that has stable and simple—or at least known—intensity and phase in both space and time. While it is possible to measure the spatial profile averaged over time and the temporal profile averaged over space, ultrafast lasers unfortunately suffer from an abundance of spatiotemporal couplings or distortions in which a pulse's temporal and spectral intensity and phase vary with transverse position, or equivalently, the spatial intensity and phase vary with time or frequency [1]. Some spatiotemporal couplings are useful in such applications as attosecond pulse generation, space–time focusing, pulse compression, and nonlinear optics [2–7], but most are not. For example, in Kerr-lens mode-locked lasers, the output mode size depends on frequency [8], and, even if it does not, it necessarily will at a focus due to the wavelength dependence of a focal spot size for a given input spot size. And since dispersive and focusing optics are ubiquitous in ultrafast laser systems, numerous additional spatiotemporal distortions, such as radial dispersion and chromatic aberration, often occur [9–12]. Also, when performing pulse compression and shaping, complex waveforms arise if the optical components become misaligned [13,14]. Furthermore, ultrashort pulses, especially, amplified ones, have extremely high intensities, so significant intensity-related nonlinear-optical effects can distort pulses as they propagate through optics [15–19]. These latter distortions are particularly problematic because they vary from shot to shot when intensity fluctuations are present, and, in ultrahigh-intensity low-repetition-rate systems, their variations from shot to shot

can be significant. As a result, a technique that can measure the complete spatiotemporal intensity-and-phase (electric field) of an ultrashort light pulse, $E(x, y, t)$, would be very useful, and, in particular, for high-intensity, low-repetition-rate pulses, a single-shot technique is essential.

Unfortunately, complete spatiotemporal characterization of ultrashort laser pulses remains extremely challenging. As mentioned above, simple, relatively uninformative measures, such as temporally averaged spatial profiles, obtained using simple cameras, are available. Over the past couple of decades, spatially averaged temporal profiles have become measurable using methods like Frequency-Resolved Optical Gating (FROG) [20]. Single-shot versions of FROG and its simpler cousin, GRENOUILLE [21,22], have also been shown to yield simple first-order spatiotemporal distortions, specifically, spatial chirp and pulse-front tilt [23,24]. However, more powerful techniques are needed to completely characterize spatiotemporally complex pulses.

More recently, a number of techniques that yield partial solutions to the spatiotemporal measurement problem have been proposed and demonstrated [1,25]. Beginning with methods that measure the temporal profile using a measured trace that is only one-dimensional (such as spectral interferometry), it is straightforward to extend the measurement using a standard two-dimensional camera to also include one spatial domain, i.e., $E(x, t)$ or $E(x, \omega)$ [26–32]. The resulting measurement, however, remains incomplete in space (either cropping or averaging over the missed spatial dimension), so assumptions must be made about the spatial homogeneity or cylindrical symmetry—which may not be valid in practice. To obtain the additional dimension, one must scan over the missed dimension.

Other techniques use combinations of spatial and temporal measurements. Shackled FROG [33,34] and HAMSTER [35] are based on combining a Hartmann–Shack spatial sensor with a FROG apparatus. The Hartmann–Shack sensor yields the spatial wavefront and amplitude information, and a FROG measurement of the central part (or anywhere else that contains all frequency components) stitches together the results. These methods are limited, however, because they must assume the same spatial phase for each monochromatic component [33] or must scan over all frequencies [36]; otherwise, the information obtained is spatially incomplete [34].

It is helpful to generate a spatiotemporally known reference pulse or train of pulses to assist with the measurement. This can be accomplished by spatially filtering a pulse to achieve a spatially simple (known) beam and then measuring the resulting essentially spatially uniform field versus time [37,38]. It is also important to verify that a train of such pulses is stable, a fact we mention here because most recently introduced temporal pulse-measurement techniques only measure the coherent artifact and so do not reveal such instability, and also yield erroneously short pulses [39,40], which would severely undermine any results when used to measure a reference pulse for a spatiotemporal measurement. In any case, the existence of a properly measured reference pulse opens up a wide range of possibilities, and a number of spatiotemporal measurement methods take advantage of this fact. Most still involve scanning in the spatial dimension(s), and the most popular include SEA TADPOLE [41] and STARFISH [42]. These methods can measure pulses completely in space and time, i.e., $E(x, y, t)$. As both of the above methods use fibers as input conduits for the probe pulses, they are inherently alignment-free and have high spatial resolution, defined only by the mode size of the fiber. However, as with all spatial or spectral scanning techniques [43–46], such methods require many shots, rendering them inapplicable for unstable or low-repetition-rate pulse trains. This is unfortunate as such pulses are usually of greater interest, especially, amplified pulses from complex systems that also more often incur nonlinear-optical spatiotemporal distortions.

As a result, we recently introduced a single-shot technique for complete spatiotemporal pulse measurement (versus x, y, and t). It is called Spatially and Temporally Resolved Intensity and Phase Evaluation Device: Full Information from a Single Hologram (STRIPED FISH) [47]. It comprises a very simple setup of a coarse two-dimensional diffractive optical element (DOE), an interference bandpass filter (IBPF), imaging optics, and a camera (see Fig. 1). It uses a spatially smoothed and temporally characterized reference pulse, accomplished at an earlier point using a spatial filter and a FROG measurement. The pulse to be measured and this known reference pulse cross at a small vertical angle on the DOE, which simultaneously generates multiple divergent pairs of beams at different angles. The DOE is also rotated slightly, so the horizontal propagation angle is different for each beam pair. Because the IBPF's transmission center wavelength varies with horizontal incidence angle, it then wavelength-filters each pair of beams to be essentially monochromatic and with different center wavelengths [48,49]. The beam pairs then overlap at the camera, generating an array of quasi-monochromatic holograms, each at a different wavelength. The spatiotemporal information of the unknown pulse is obtained from the multiple
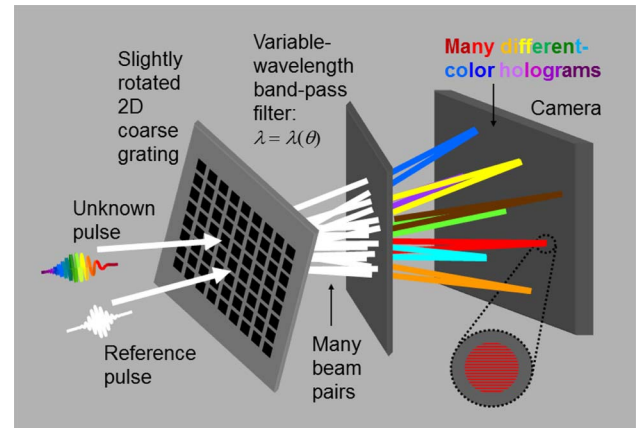

Fig. 1.   Conceptual schematic of STRIPED FISH.

holograms and from the knowledge of the reference pulse, yielding a complete measurement on a single camera frame, and hence, if desired, on a single shot.

In its initial demonstration [50], STRIPED FISH successfully measured simple temporally and spatially chirped pulses. Even for such simple pulses, however, the resulting data set is necessarily quite large: two four-dimensional arrays, which contain the intensity and phase versus x, y, and t. Thus, in order to display the measured pulses in still images, we had to suppress one spatial dimension, and so we used a two-dimensional surface (versus x and t or y and t), whose height represented intensity and color represented the instantaneous frequency. In addition, we made movies that displayed the pulse intensity and instantaneous frequency versus x and y, in which real time indicated pulse time, but slowed by 14 orders of magnitude.

2. ISSUES

As with any new device, the initial implementation of STRIPED FISH had limitations.

A. Spectral Range
The transmitted central wavelength of an IBPF depends approximately linearly on the beam incidence angle. As a result, a STRIPED FISH device's spectral range is limited by the range of beam angles impinging on the IBPF, which itself is limited by the range of angles generated by the DOE. In order to increase the device spectral range (previously ∼20 nm), a smaller feature size of the DOE, thus, a larger range of beam angles emerging from it, is required.

B. Aberrations
When the pairs of beams emerging from the DOE diverge more, they must be imaged from the DOE to the camera with a magnification significantly less than unity because the pattern quickly becomes too large to fit on a standard camera. Such large-angle imaging with simple lenses, however, results in severe aberrations (especially, barrel distortion) due to the highly off-axis propagation. Holograms at the left and right edges of the trace that correspond to beams that are spatially Gaussian appear stretched or comet-shaped, likely due to coma, and retrieving an accurate spatial intensity pattern for the reddest and bluest wavelengths becomes difficult.

C. Order Inequality

The various holograms had inherently highly unequal intensities (low orders were generally more intense) due to the usual order-dependent diffraction efficiency at the DOE. When the beam was attenuated enough that the central holograms did not saturate the camera, the peripheral holograms were very faint and had a low signal-to-noise ratio. Of course, a higher-dynamic-range camera could help here, but it is expensive.

D. Very Bright Central Zero-Order Artifact

The useful holograms were accompanied by a strong and useless undiffracted central artifact, which overwhelmed adjacent holograms. This zero-order central-spike artifact [50] was due to the reflection from the substrate of the DOE, which consisted of mostly transparent regions with small, square reflective coatings. An attempt to eliminate this artifact involved operating in reflection at the Brewster's angle of the substrate. It effectively removed the central-spike artifact, but it also, unfortunately, introduced a weak "ghost" reflection from the back surface of the substrate [50]. Moreover, operating the subsequent imaging system at such an oblique angle (Brewster's angle) was vulnerable to off-axis misalignment and suffered from astigmatism.

E. Display Method for the Measured Pulse

Finally, even the seemingly simple task of plotting the measured pulse proved quite challenging, due to the inherent data volume of both the intensity and phase versus x, y, and t (i.e., two four-dimensional graphs). Previously [51], to show the time evolution, we either suppressed a dimension or made movies by plotting the intensity and instantaneous frequency as functions of x and y, and slowing time by ~14 orders of magnitude. While these movies displayed simple chirped pulses well, the instantaneous frequency can, in practice, be highly unnatural in appearance: white regions of pulses (where all frequencies are present) are displayed as green —a well-known fundamental problem of the instantaneous-frequency concept.

3. IMPROVEMENTS

To solve these problems, we have made several improvements. First, we have converted to a normal-incidence "negative DOE," whose transmission function is equal to the reflection function of the previous DOE. Therefore, this new grating has the same diffraction pattern in transmission as before in reflection. But, as it works in a transmission manner, it has no zero-order central-spike artifact or "ghost" reflection.

Second, we added an apodizing neutral-density filter (ANDF), placed near the focal plane of the first lens [see Fig. 2(a)]. Its radially decreasing optical density significantly attenuates central beams (low diffraction orders) relative to the peripheral ones (high orders). As a result, it better balances the intensities of the various diffracted orders, as can be seen by comparing Figs. 2(b) and 2(d).

At large incidence angles, aberrations become more problematic. So, third, to collect the more highly divergent beams and to direct them to the camera without barrel distortion (and any less visible, but potentially deleterious), we added an imaging system comprising two highly aberration-corrected
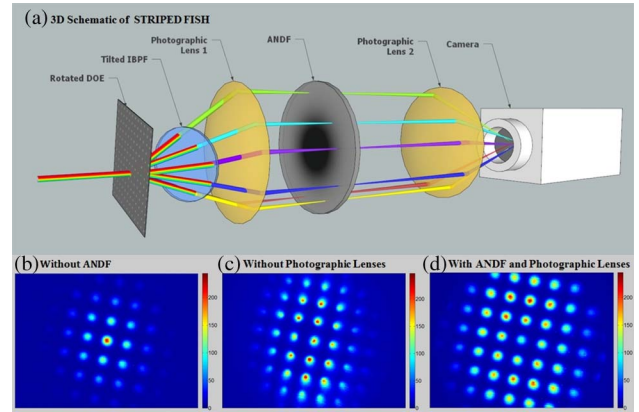

Fig. 2. Improved STRIPED FISH apparatus and camera shots, showing the effect of the ANDF and photographic lenses, when only the unknown beam is incident (that is, without a reference beam). (a) 3D schematic of the STRIPED FISH apparatus. The input broadband beam is split into multiple quasi-monochromatic beams and is then imaged onto the camera. (b) Camera shot without the ANDF. Note that, due to the diffraction efficiencies and the pulse spectrum, the central spot appears much brighter than the peripheral ones (27.3 times difference in peak intensity). (c) Camera shot imaged using two simple convex lenses (that is, not using photography lenses). Note the barrel-like beam array with irregular spot shapes, due to the aberrations of the singlet lenses. (d) Camera shot after incorporating the ANDF and photographic lenses. Note the increased peripheral visibility (5.7 times peak intensity difference) and suppressed aberrations, resulting in a good signal-to-noise ratio for a wider range of wavelengths.

commercial photographic lenses. Such lenses are designed for large incidence angles, as are common in photography, and they are corrected for a wide range of aberrations. These lenses successfully image the divergent beams with minimal aberrations [when we compare Fig. 2(c) with Fig. 2(d), the former shows the barrel distortion of the beam pattern and highly irregular beam shapes]. This allows a greater range of angles at the IBPF and, therefore, a larger wavelength range. Although these multi-element lenses contain significant amounts of glass, they can be used in our ultrafast optical device because the resulting group-delay dispersion is experienced by both the unknown and reference pulses, and so, cancels out of the holographic measurement.

With these improvements, up to 40 holograms could be imaged onto a 10.5 mm × 7.73 mm camera chip with negligible aberrations. This increased the spectral range and allowed the device to use the full dynamic range of the camera (8 bits, 0–255) with a reasonable signal-to-noise ratio for all holograms.

As a side note, although we use the holograms to obtain the intensity and phase of the pulse here, note also that if the reference beam is absent and only the unknown beam is incident, STRIPED FISH behaves exactly as a single-frame low-resolution three-dimensional (3D) imaging spectrometer [see Fig. 2(a)], yielding at the camera the spatially dependent spectrum, $I(x, y, \omega)$. This may be of interest for spectroscopic applications [52,53].

To more intuitively display the measured intensity and phase (versus x, y, and t), we no longer use the instantaneous frequency, and now instead, compute the numerical spectrograms [see Eq. (1)] of the retrieved pulse at each point in space using a numerically generated variably delayed gate pulse (a fraction of a pulse length long). This approach

simulates that of the human eye if it had the temporal resolution to see the pulse evolving. The expression for these spectrograms is

$$Sp(x, y, T, \omega) = \left| \int_{-\infty}^{\infty} E(x, y, t) g(t - T) \exp(-i\omega t) \mathrm{d}t \right|^2, \quad (1)$$

where $g(t - T)$ is the numerical gate function with variable delay T.

We then compute the overlap integrals of each spectrogram with red, green, and blue response functions:

$$R(x, y, T) = \int_{-\infty}^{\infty} Sp(x, y, T, \omega) R(\omega) \mathrm{d}\omega, \quad (2)$$

where $R(\omega)$ is (for example) a red response function. This function is a simple Gaussian centered at a red frequency if true color is desired. If false color is desired, then this function is centered on the longer-wavelength colors of the pulse spectrum. Similar response functions are used to compute the green (or center for false color) and blue (or shorter-wavelength) overlap integrals. The resulting color functions then serve as RGB values (versus x, y, and t), ensuring that a pixel appears white at places and times when the whole spectrum is present, and red/blue biased when longer/shorter wavelengths dominate. Also, we normalize the total color contents, so that the brightness (weight of color) represents the relative intensity (versus x, y, and t). Since the color of the pixels represents phase, both the intensity and phase information is contained in the RGB functions. This allows us to generate color movies as the human eye would perceive the pulse if the eye actually had the temporal resolution to do so.

4. RETRIEVING THE PULSE FROM STRIPED FISH HOLOGRAMS

To measure an unknown pulse, we first temporally characterize a spatially filtered simple pulse, $E_r(x, y, \omega)$, obtaining the required spatiotemporally known reference pulse. This pulse then crosses with the unknown pulse, $E_u(x, y, \omega)$, at a small vertical angle α, forming an interfering beam pair. By passing through the DOE and the IBPF, holograms of many different frequencies are generated. Afterward, the imaging system relays the holograms onto the camera. The interference of the reference and unknown pulses at each frequency is given by

$$I(x, y, \omega) = |E_u(x, y, \omega)|^2 + |E_r(x, y, \omega)|^2$$
$$+ E_u(x, y, \omega) E_r(x, y, \omega)^* \exp(+iky\sin(\alpha))$$
$$+ E_r(x, y, \omega) E_u(x, y, \omega)^* \exp(-iky\sin(\alpha)), \quad (3)$$

where the asterisk denotes the complex conjugate. Note that all amplitude and phase information of the unknown pulse is contained within the oscillating term $E_u(x, y, \omega) E_r(x, y, \omega)^* \exp(+iky\sin(\alpha))$, where the "carrier" $\exp(+iky\sin(\alpha))$ is easily removed to retrieve the "envelope" $E_u(x, y, \omega) E_r(x, y, \omega)^*$ by a Fourier-filtering algorithm [54]. Furthermore, because $E_r(x, y, \omega)$ is known, the complex unknown spatiospectral field $E_u(x, y, \omega)$ is then obtained. By performing an inverse Fourier transform (IFT) for each location, we obtain
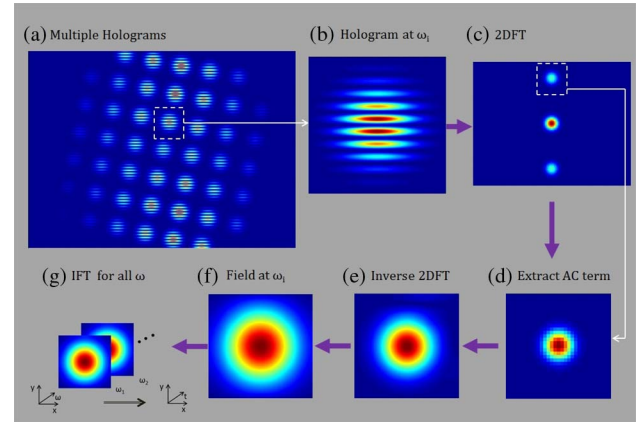

Fig. 3.   Illustration of the STRIPED FISH retrieval algorithm. Amplitudes are plotted for complex quantities. (a) Multiple holograms of different frequencies are recorded on the camera. (b) Hologram of a certain frequency ω_i is selected. (c) Two-dimensional Fourier transform (2DFT) is taken over spatial dimensions. (d) The oscillating alternating current (AC) term is extracted. (e) Inverse 2DFTs into the space (x, y) domain, obtaining a product term. (f) Dividing the reference field to obtain the unknown spatial field at ω_i, $E_u(x, y, \omega_i)$. (g) Performing (a)–(f) for every hologram yields $E_u(x, y, \omega)$, then $E_u(x, y, t)$ by an IFT into the time domain.

the unknown field in the spatiotemporal domain, $E_u(x, y, t)$. To illustrate this, we demonstrate the retrieval of a positively chirped Gaussian pulse, following proper calibration parameters, from a simulated trace, as shown in Fig. 3.

5. EXPERIMENTAL SETUP

To demonstrate the effects of these improvements, we performed measurements on spatiotemporally complex pulses. We also used a high-repetition-rate oscillator, so the measurements were not truly single-shot, but we used only a single camera frame, yielding a proof of principle that true single-shot measurements are possible. As shown in Fig. 4, the output from a Ti:sapphire oscillator (KMLabs, 800 nm center wavelength, 20 nm in FWHM, extending toward the ~50 nm
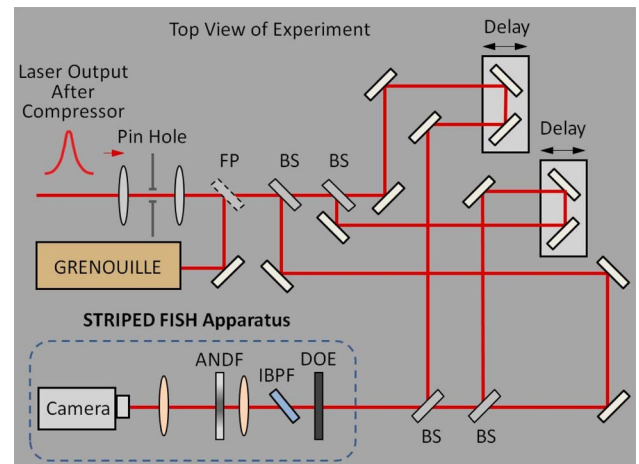

Fig. 4.   Top view of the current experiment for generating and measuring a complex unknown pulse consisting of two crossed, delayed, and chirped pulses. Chirp was controlled by the pulse compressor. An FP was used to switch the beam to the GRENOUILLE. Three BSs provided the reference and double pulse to be measured. The STRIPED FISH device is shown on the lower left in the dashed blue frame.

range) is propagated through a pulse compressor (Swamp Optics BOA Compressor) and then through a spatial filter made of two convex lenses (first, 300 mm; second, 100 mm) and a pinhole (75 μm). A flip mirror (FP) was then used to switch the beam path into the GRENOUILLE (Swamp Optics, model 8-50). When the FP was flipped out of the beam, the beam propagated into two sets of beam splitters (BSs) that divided it into three replicas. One acted as the reference pulse and the other two were combined at different angles with varying amounts of chirp and delay, creating a double pulse with chirped-pulse beating that varied with spatial position. Two delay stages were used to synchronize the two unknown pulses and the reference.

The coarse DOE was made by photomasking a soda lime substrate with a dark-field chrome coating, which comprised an array of transparent square windows (3 μm × 3 μm, 15 μm spacing) that diffracted the beams into highly divergent (∼30°) beam arrays. The DOE was slightly rotated (∼10°) in the vertical plane to ensure that different beam replicas all propagated at different horizontal angles. Then the beams were spectrally resolved by an IBPF (Semrock LL01-852, 3.2 nm bandwidth, but tilted by ∼40°, which increased the bandwidth to ∼5 nm), with their center wavelength determined by their incidence angles. In this way, the whole spectrum of interest (∼775 to ∼825 nm) could be measured, with all frequencies calibrated by a fiber-coupled spectrometer (Ocean Optics HR4000). The imaging system consisted of two photographic lenses (lens 1: Computar c-mount 50 mm, ƒ1.8; lens 2: Computar c-mount 75 mm, ƒ1.4) and an ANDF (Edmund Optics 64386). After the imaging system, the unknown double pulses interfered with the reference pulses on the camera screen (PixeLINK PL-A781, 3000 × 2208 pixels, 3.5 μm pixel pitch), forming ∼40 quasi-monochromatic (∼5 nm bandwidth) holograms at different frequencies.

6. RESULTS AND SIMULATIONS

Using the setup above, we measured spatiotemporally complex pulses consisting of double pulses crossed at various angles and with varying amounts of delay and chirp. Figure 5(a) shows the resulting camera frame containing the multiple holograms generated by the interference of the unknown and reference beams at different frequencies. Figure 5(b) shows a camera image of only the unknown double pulse (with the reference beam blocked), yielding the spatial intensities for various frequencies, $I_u(x, y, \omega)$. Figures 5(c) and 5(d) show simulated camera frames for Figs. 5(a) and 5(b), respectively, assuming Gaussian beams with the actual known beam-crossing angle, relative delay, pulse chirp, and spectral response parameters. A comparison shows that the measured camera frames agree well with what is expected based on our knowledge of the pulse's electric field.

For each measurement, we generated a false-color STRIPED FISH-measured movie of $E_u(x, y, t)$. The movie shows the spatially and temporally complex brightness and color patterns for the unknown crossing double pulses. Also, to ensure the credibility of our measured results, we have performed two cross-checks. The first check was a STRIPED FISH internal check: a STRIPED FISH measurement was performed for each individual pulse that constituted the unknown double pulse, and then their electric fields retrieved were added numerically, using the known crossing angle
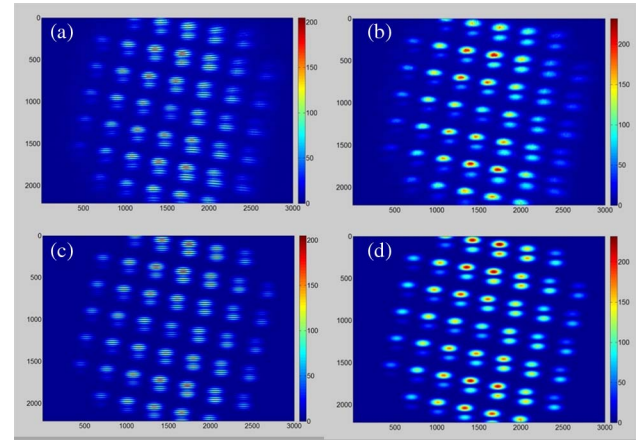

Fig. 5.   STRIPED FISH traces and unknown pulse spectra for 28.9-fs-spaced, 122.1-fs-long positively chirped double pulses crossing at a small angle (∼0.1°). Color shows the intensity. x and y axes are in pixels. (a) Holograms created by the interference of the reference and unknown double pulses on the camera screen. (b) Blocking the reference pulse yields the unknown pulse spatial profiles for each frequency, $I_u(x, y, \omega)$. (c) Simulated STRIPED FISH trace. (d) Simulated unknown-pulse spatial profiles for each frequency, $I_u(x, y, \omega)$.

and delay, to yield the unknown field. The double-pulse field (movie) obtained in this way should be the same as that from the direct measurement of both pulses at once. A second check was to perform a theoretical simulation of the STRIPED FISH trace assuming simple Gaussian pulse and beam shapes, and their known crossing angles and delays. Again, the simulated movie is expected to have features similar to that of the directly measured one.

For demonstration, we first show the movies of crossing chirped pulses with 0 relative delay. In this case, we expect spatial fringes consistent with the crossing pulses, and only the color of the pulse should change with time. Figure 6 shows the movies of the positively chirped crossing pulses, while Fig. 7 shows those of the negatively chirped pulses. All relative delay values are obtained by linear fitting of the measured
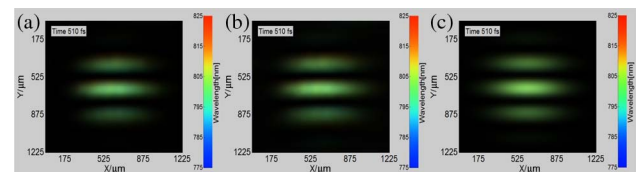

Fig. 6.   Movies of STRIPED FISH-measured double pulses comprising two 122.1-fs-long positively chirped pulses with a 2.3 fs separation and crossing at a small angle (∼0.1°). The relative time is shown in the upper left corner. (a) STRIPED FISH-measured result (Media 1). (b) Internal check result (Media 2). (c) Simulation result (Media 3).
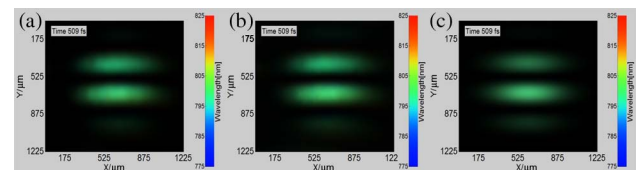

Fig. 7.   Movies of STRIPED FISH-measured double pulses comprising two 122.7-fs-long negatively chirped pulses with a 0.8 fs separation and crossing at a small angle (∼0.1°). The relative time is shown in the upper left corner. (a) STRIPED FISH-measured result (Media 4). (b) Internal check result (Media 5). (c) Simulation result (Media 6).
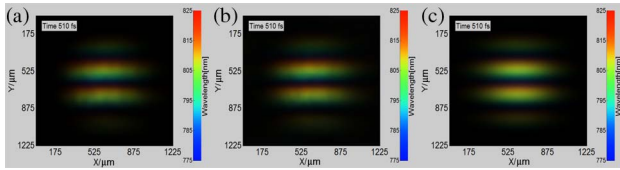
Fig. 8.   Movies of STRIPED FISH-measured double pulses comprising two 122.1-fs-long positively chirped pulses with a 39.6 fs separation and crossing at a small angle (~0.1°). The relative time is shown in the upper left corner. (a) Measured result (Media 7). (b) Internal check result (Media 8). (c) Simulation result (Media 9).
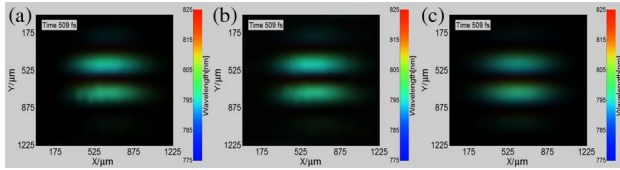

Fig. 9.   Movies of STRIPED FISH-measured double pulses comprising two 122.7-fs-long negatively chirped pulses with a 28.1 fs separation and crossing at a small angle (~0.1°). The relative time is shown in the upper left corner. (a) Measured result (Media 10). (b) Internal check result (Media 11). (c) Simulation result (Media 12).

Fig. 10.   Movies of STRIPED FISH-measured interference between 2.3-fs-spaced, 122.1-fs-long positively chirped double pulses crossing at a smaller angle. The relative time is shown in the upper left corner. (a) Measured result (Media 13). (b) Internal check result (Media 14). (c) Simulation result (Media 15).

Fig. 11.   Movies of STRIPED FISH-measured interference between 28.9-fs-spaced, 122.1-fs-long positively chirped double pulses crossing at a smaller angle. The relative time is shown in the upper left corner. (a) Measured result (Media 16). (b) Internal check result (Media 17). (c) Simulation result (Media 18).

relative phase between the centers of the unknown double pulses.

Next, the relative delay between the two pulses in the unknown double pulse was adjusted from ~0 to ~30fs with a high-precision motorized translation stage (Newport ESP UE16PP, 0.074 μm resolution). As expected, adding a delay between the pulses causes chirped-pulse beating. Since the exact delay between the pulses varies with spatial position due to the crossing angle, different colors experience constructive interference at different positions. As a result, the fringes move and change colors with time in interesting ways. Figure 8 shows the movie results for the positively chirped pulses, while Fig. 9 shows the results for the negatively chirped pulses.

Then, in a second set of measurements, the angle between the pulses was decreased in order to vary the spatial interference pattern. Figure 10 shows the result for pulses
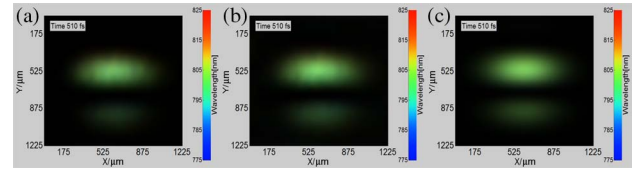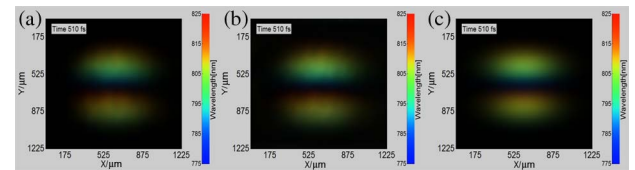
that are essentially coincident in time. As expected, decreasing the angle between the beams results in an interference pattern with broader fringes. The transverse variation in delay between the beams is smaller, so when a ~30 fs delay is added between the pulses, the chirped-pulse-beating pattern varies more slowly as a function of position (see Fig. 11).

Once the four-dimensional field of $E_u(x, y, t)$ is obtained, we can always suppress one dimension (say, x axis), by fixing on a particular coordinate value (say, x_c), and get conventional 3D figures. As an example, in Fig. 12, we have plotted the spatiotemporal field $E_u(x, y, t)$, as the one in Fig. 6(a), for several different time points (427, 521, and 594 fs), together with the frames of the simulated field $E_{sim}(x, y, t)$, as the one in Fig. 6(c). From these figures, we can see that the Gaussian-pulse simulated results match well with the actual measured results.
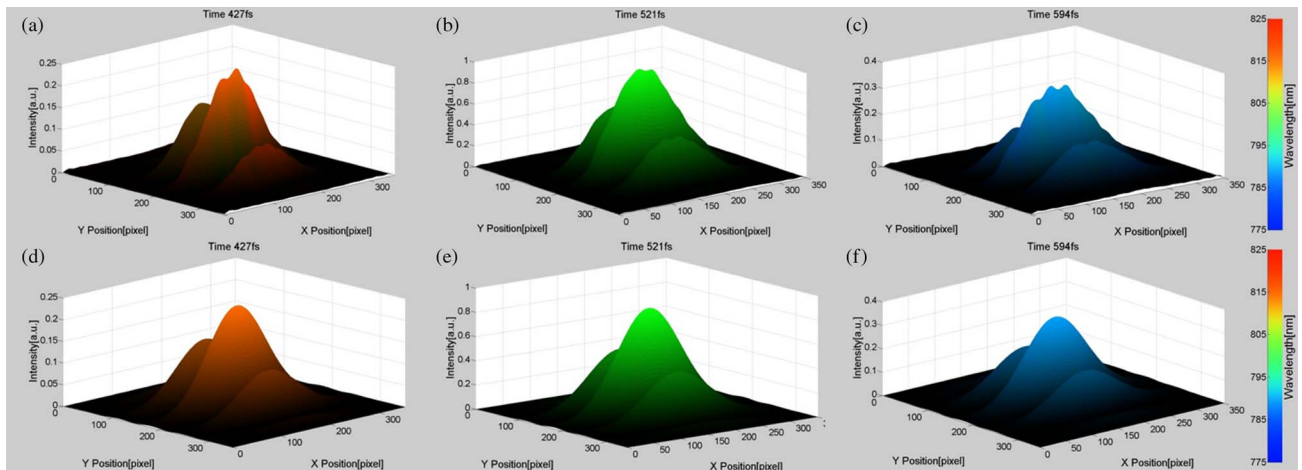

Fig. 12.   Spatiotemporal field at different time points for two 2.3-fs-spaced, 122.1-fs-long positively chirped double pulses crossing at a small angle (~0.1°), as the one in Fig. 6(a). The height and brightness scale with the intensity and the color represents the frequency. (a) Measured field at 427 fs. (b) Measured field at 521 fs. (c) Measured field at 594 fs. (d) Simulated field at 427 fs. (e) Simulated field at 521 fs. (f) Simulated field at 594 fs.

7. DISCUSSION

Our measured and simulated results confirm that STRIPED FISH accurately measures pulses showing complex spatio-temporal behavior. For crossing double pulses, STRIPED FISH was able to retrieve the intensity and phase correctly, even for the low-intensity regions between the fringes. Several megapixels of data were used for retrieval ($350 \times 350 \times 35$) from a single camera frame, together with the FROG measurement, ensuring relatively high resolutions in space and time (frequency). Nevertheless, not all details in the retrieved traces and movies achieved perfect agreement with the simulations. For example, there are minor intensity discrepancies in the traces, and the simulated movies appear more spatially smooth than the measured movies. Possible reasons for these discrepancies include the assumed Gaussian profile used for the reference pulse and the finite filter bandwidth.

Further improvements to the device could involve extension to more complex pulses, which would require scaling up the number of holograms, by, for example, using a larger camera sensor. Also, a higher-dynamic-range camera combined with an ANDF could yield an even better signal-to-noise ratio in the holograms. Extension to longer pulses would require increasing the spectral resolution, which would be difficult in view of currently available filter bandwidths, angular dispersion's tendency to spatially smear the resulting holograms, and the resulting increase in the divergence of the many beams after the DOE. On the other hand, this device should be easily adapted to other wavelength ranges by selecting relevant parameters for the DOE, IBPF, and imaging system. As a result, in its current form, STRIPED FISH should be able to measure most visible and infrared ultrashort pulses of interest.

8. CONCLUSIONS

We have demonstrated an improved STRIPED FISH device for measuring a spatiotemporally complex pulse. STRIPED FISH is, to the best of our knowledge, the first apparatus to yield a complete spatiotemporal electric field in all three dimensions, x, y, and t (z information is not needed, as it can then be obtained using the Fresnel integral), for an ultrashort pulse on a single camera frame. Thus, this device should be able to measure complex pulses on a single shot using its compact optics, without complicated alignment or scanning issues. The new DOE, IBPF, and imaging optics work together to increase the spectral range by generating a larger divergence angle among the beams ($\sim$50 nm, $\sim$30$°$ compared with $\sim$20 nm, $\sim$10$°$ in previous work), with negligible aberrations. Also, the apodizing filter significantly improved the intensity uniformity for the numerous holograms generated in the device. With the spectrogram-based movies, STRIPED FISH now provides a visually intuitive movie to demonstrate the intensity and phase of the measured pulse over space and time. As an example, we showed that STRIPED FISH can measure the fairly complex intensity and phase behavior of crossing chirped double pulses, from a Ti:sapphire oscillator, with various delays, chirps, and crossing angles. We performed cross-checks to test the retrieval robustness, which agreed well with directly measured results.

ACKNOWLEDGMENTS

REFERENCES

1. S. Akturk, X. Gu, P. Bowlan, and R. Trebino, "Spatio-temporal couplings in ultrashort laser pulses," J. Opt. **12**, 093001 (2010).
2. J. A. Wheeler, A. Borot, S. Monchocé, H. Vincenti, A. Ricci, A. Malvache, R. Lopez-Martens, and F. Quéré, "Attosecond lighthouses from plasma mirrors," Nat. Photonics **6**, 829–833 (2012).
3. S. Mao, F. Quéré, S. Guizard, X. Mao, R. Russo, G. Petite, and P. Martin, "Dynamics of femtosecond laser interactions with dielectrics," Appl. Phys. A **79**, 1695–1709 (2004).
4. C. G. Durfee, M. Greco, E. Block, D. Vitek, and J. A. Squier, "Intuitive analysis of space-time focusing with double-ABCD calculation," Opt. Express **20**, 14244–14259 (2012).
5. V. Chauhan, P. Bowlan, J. Cohen, and R. Trebino, "Single-diffraction-grating and grism pulse compressors," J. Opt. Soc. Am. B **27**, 619–624 (2010).
6. B. A. Richman, S. E. Bisson, R. Trebino, E. Sidick, and A. Jacobson, "All-prism achromatic phase matching for tunable second-harmonic generation," Appl. Opt. **38**, 3316–3323 (1999).
7. T. C. Wong and R. Trebino, "Single-frame measurement of complex laser pulses tens of picoseconds long using pulse-front tilt in cross-correlation frequency-resolved optical gating," J. Opt. Soc. Am. B **30**, 2781–2786 (2013).
8. S. Cundiff, E. Ippen, H. Haus, and W. Knox, "Frequency-dependent mode size in broadband Kerr-lens mode locking," Opt. Lett. **21**, 662–664 (1996).
9. Z. Bor, "Distortion of femtosecond laser pulses in lenses and lens systems," J. Mod. Opt. **35**, 1907–1918 (1988).
10. P. Bowlan, P. Gabolde, and R. Trebino, "Directly measuring the spatio-temporal electric field of focusing ultrashort pulses," Opt. Express **15**, 10219–10230 (2007).
11. M. Kempe and W. Rudolph, "Femtosecond pulses in the focal region of lenses," Phys. Rev. A **48**, 4721–4729 (1993).
12. J. Jasapara and W. Rudolph, "Characterization of sub-10-fs pulse focusing with high-numerical-aperture microscope objectives," Opt. Lett. **24**, 777–779 (1999).
13. C. Fiorini, C. Sauteret, C. Rouyer, N. Blanchot, S. Seznec, and A. Migus, "Temporal aberrations due to misalignments of a stretcher–compressor system and compensation," IEEE J. Quantum Electron. **30**, 1662–1670 (1994).
14. G. Pretzler, A. Kasper, and K. Witte, "Angular chirp and tilted light pulses in CPA lasers," Appl. Phys. B **70**, 1–9 (2000).
15. H. Kumagai, S.-H. Cho, K. Ishikawa, K. Midorikawa, M. Fujimoto, S.-i. Aoshima, and Y. Tsuchiya, "Observation of the complex propagation of a femtosecond laser pulse in a dispersive transparent bulk material," J. Opt. Soc. Am. B **20**, 597–602 (2003).
16. A. Matijošius, P. Di Trapani, A. Dubietis, R. Piskarskas, A. Varanavičius, and A. Piskarskas, "Nonlinear space–time dynamics of ultrashort wave packets in water," Opt. Lett. **29**, 1123–1125 (2004).
17. D. Faccio, M. A. Porras, A. Dubietis, F. Bragheri, A. Couairon, and P. Di Trapani, "Conical emission, pulse splitting, and *X*-wave parametric amplification in nonlinear dynamics of ultrashort light pulses," Phys. Rev. Lett. **96**, 193901 (2006).
18. A. Couairon and A. Mysyrowicz, "Femtosecond filamentation in transparent media," Phys. Rep. **441**, 47–189 (2007).
19. D. E. Adams, T. A. Planchon, A. Hrin, J. A. Squier, and C. G. Durfee, "Characterization of coupled nonlinear spatiospectral phase following an ultrafast self-focusing interaction," Opt. Lett. **34**, 1294–1296 (2009).
20. R. Trebino, *Frequency-Resolved Optical Gating: The Measurement of Ultrashort Laser Pulses* (Kluwer Academic, 2002).
21. P. O'Shea, M. Kimmel, X. Gu, and R. Trebino, "Highly simplified device for ultrashort-pulse measurement," Opt. Lett. **26**, 932–934 (2001).
22. S. Akturk, M. Kimmel, P. O'Shea, and R. Trebino, "Extremely simple device for measuring 20-fs pulses," Opt. Lett. **29**, 1025–1027 (2004).
23. S. Akturk, M. Kimmel, P. O'Shea, and R. Trebino, "Measuring spatial chirp in ultrashort pulses using single-shot Frequency-Resolved Optical Gating," Opt. Express **11**, 68–78 (2003).

24. S. Akturk, M. Kimmel, P. O'Shea, and R. Trebino, "Measuring pulse-front tilt in ultrashort pulses using GRENOUILLE," Opt. Express **11**, 491–501 (2003).

25. I. A. Walmsley and C. Dorrer, "Characterization of ultrashort electromagnetic pulses," Adv. Opt. Photon. **1**, 308–437 (2009).

26. F. Bragheri, D. Faccio, F. Bonaretti, A. Lotti, M. Clerici, O. Jedr-kiewicz, C. Liberale, S. Henin, L. Tartara, and V. Degiorgio, "Complete retrieval of the field of ultrashort optical pulses using the angle-frequency spectrum," Opt. Lett. **33**, 2952–2954 (2008).

27. S. Kahaly, S. Monchocé, V. Gallet, O. Gobert, F. Réau, O. Tcherbakoff, P. D'Oliveira, P. Martin, and F. Quéré, "Investigation of amplitude spatio-temporal couplings at the focus of a 100 TW–25 fs laser," Appl. Phys. Lett. **104**, 054103 (2014).

28. C. Dorrer, E. Kosik, and I. Walmsley, "Direct space time-characterization of the electric fields of ultrashort optical pulses," Opt. Lett. **27**, 548–550 (2002).

29. C. Dorrer, E. Kosik, and I. Walmsley, "Spatio-temporal characterization of the electric field of ultrashort optical pulses using two-dimensional shearing interferometry," Appl. Phys. B **74**, s209–s217 (2002).

30. L. Gallmann, G. Steinmeyer, D. Sutter, T. Rupp, C. Iaconis, I. Walmsley, and U. Keller, "Spatially resolved amplitude and phase characterization of femtosecond optical pulses," Opt. Lett. **26**, 96–98 (2001).

31. A. S. Wyatt, I. A. Walmsley, G. Stibenz, and G. Steinmeyer, "Sub-10 fs pulse characterization using spatially encoded arrangement for spectral phase interferometry for direct electric field reconstruction," Opt. Lett. **31**, 1914–1916 (2006).

32. E. M. Kosik, A. S. Radunsky, I. A. Walmsley, and C. Dorrer, "Interferometric technique for measuring broadband ultrashort pulses at the sampling limit," Opt. Lett. **30**, 326–328 (2005).

33. F. Bonaretti, D. Faccio, M. Clerici, J. Biegert, and P. Di Trapani, "Spatiotemporal amplitude and phase retrieval of Bessel-*X* pulses using a Hartmann–Shack sensor," Opt. Express **17**, 9804–9809 (2009).

34. E. Rubino, D. Faccio, L. Tartara, P. K. Bates, O. Chalus, M. Clerici, F. Bonaretti, J. Biegert, and P. Di Trapani, "Spatiotemporal amplitude and phase retrieval of space–time coupled ultrashort pulses using the Shackled-FROG technique," Opt. Lett. **34**, 3854–3856 (2009).

35. S. L. Cousin, J. M. Bueno, N. Forget, D. R. Austin, and J. Biegert, "Three-dimensional spatiotemporal pulse characterization with an acousto-optic pulse shaper and a Hartmann–Shack wave-front sensor," Opt. Lett. **37**, 3291–3293 (2012).

36. C. Hauri, J. Biegert, U. Keller, B. Schaefer, K. Mann, and G. Marowski, "Validity of wave-front reconstruction and propagation of ultrabroadband pulses measured with a Hartmann–Shack sensor," Opt. Lett. **30**, 1563–1565 (2005).

37. W. Amir, T. A. Planchon, C. G. Durfee, J. A. Squier, P. Gabolde, R. Trebino, and M. Müller, "Simultaneous visualization of spatial and chromatic aberrations by 2D Fourier transform spectral interferometry," Opt. Lett. **31**, 2927–2929 (2006).

38. W. Amir, T. Planchon, C. Durfee, and J. Squier, "Complete characterization of a spatiotemporal pulse shaper with two-dimensional Fourier transform spectral interferometry," Opt. Lett. **32**, 939–941 (2007).

39. J. Ratner, G. Steinmeyer, T. C. Wong, R. Bartels, and R. Trebino, "Coherent artifact in modern pulse measurements," Opt. Lett. **37**, 2874–2876 (2012).

40. M. Rhodes, G. Steinmeyer, J. Ratner, and R. Trebino, "Pulse-shape instabilities and their measurement," Laser Photon. Rev. **7**, 557–565 (2013).

41. P. Bowlan, P. Gabolde, A. Shreenath, K. McGresham, R. Trebino, and S. Akturk, "Crossed-beam spectral interferometry: a simple, high-spectral-resolution method for completely characterizing complex ultrashort pulses in real time," Opt. Express **14**, 11892–11900 (2006).

42. B. Alonso, Í. J. Sola, Ó. Varela, J. Hernández-Toro, C. Méndez, J. San Román, A. Zaïr, and L. Roso, "Spatiotemporal amplitude-and-phase reconstruction by Fourier-transform of interference spectra of high-complex-beams," J. Opt. Soc. Am. B **27**, 933–940 (2010).

43. F. Eilenberger, A. Brown, S. Minardi, and T. Pertsch, "Imaging cross-correlation FROG: measuring ultrashort, complex, spatio-temporal fields," Opt. Express **21**, 25968–25976 (2013).

44. J. Trull, O. Jedrkiewicz, P. Di Trapani, A. Matijosius, A. Varanavicius, G. Valiulis, R. Danielius, E. Kucinskas, A. Piskarskas, and S. Trillo, "Spatiotemporal three-dimensional mapping of nonlinear *X* waves," Phys. Rev. **69**, 026607 (2004).

45. B. Alonso, I. J. Sola, O. Varela, C. Méndez, I. Arias, J. San Román, A. Zaïr, and L. Roso, "Spatio-temporal characterization of laser pulses by spatially resolved spectral interferometry," Opt. Pura Apl. **43**, 1–7 (2010).

46. N. Mehta, C. Yang, Y. Xu, and Z. Liu, "Characterization of the spatiotemporal evolution of ultrashort optical pulses using FROG holography," Opt. Express **22**, 11099–11106 (2014).

47. P. Gabolde and R. Trebino, "Single-shot measurement of the full spatiotemporal field of ultrashort pulses with multi-spectral digital holography," Opt. Express **14**, 11460–11467 (2006).

48. M. Bass, E. W. Van Stryland, D. R. Williams, and W. L. Wolfe, *Handbook of Optics. Fundamentals, Techniques, and Design* (McGraw-Hill, 1995), Vol. **1**.

49. P. Lissberger and W. Wilcock, "Properties of all-dielectric interference filters. II. Filters in parallel beams of light incident obliquely and in convergent beams," J. Opt. Soc. Am. **49**, 126–128 (1959).

50. P. Gabolde and R. Trebino, "Single-frame measurement of the complete spatio-temporal intensity and phase of ultrashort laser pulse(s) using wavelength-multiplexed digital holography," J. Opt. Soc. Am. B **25**, A25–A33 (2008).

51. P. Gabolde and R. Trebino, "Self-referenced measurement of the complete electric field of ultrashort pulses," Opt. Express **12**, 4423–4429 (2004).

52. Y. Garini, I. T. Young, and G. McNamara, "Spectral imaging: principles and applications," Cytometry **69**, 735–747 (2006).

53. N. Gat, "Imaging spectroscopy using tunable filters: a review," Proc. SPIE **4056**, 50–64 (2000).

54. M. Takeda, H. Ina, and S. Kobayashi, "Fourier-transform method of fringe-pattern analysis for computer-based topography and interferometry," J. Opt. Soc. Am. A **72**, 156–160 (1982).